

Dynamical study of ion-beam oxidation: Incorporation of hyperthermal oxygen ions into silicon oxide thin films

T. Tzvetkov, X. Qin, and D. C. Jacobs

Department of Chemistry and Biochemistry, University of Notre Dame, Notre Dame, Indiana 46556

(Received 22 August 2002; published 28 February 2003)

The complex dynamics associated with ion-beam oxidation of Si(001) by 5–100-eV O^+ and O_2^+ is studied *in situ*. Room-temperature oxidation of silicon under ultrahigh vacuum conditions is accomplished with a mass-selected, monoenergetic, oxygen ion beam. Initially, a thin $Si^{16}O_x$ film is prepared by bombarding clean Si(001) with hyperthermal energy $^{16}O^+$. Switching the incident ion flux to $^{18}O^+$ or $^{36}O_2^+$ creates an isotopically labeled tracer for monitoring the rate at which subsequent incident oxygen ions are incorporated into the topmost layer of the growing silicon oxide film. The cross section for oxygen incorporation is found to depend strongly on (i) the conditions under which the underlying oxide layer was grown, (ii) the kinetic energy of the incorporating ion, and (iii) whether the incident ion is atomic or molecular oxygen.

DOI: 10.1103/PhysRevB.67.075418

PACS number(s): 68.47.Gh, 68.49.Sf, 81.15.Jj, 81.65.Mq

I. INTRODUCTION

The reaction of hyperthermal energy ions with surfaces presents enormous opportunities for achieving chemical control.¹ Hyperthermal translational energies (5–500 eV) are sufficient to activate a wide variety of chemical transformations at the gas/surface interface including abstraction, oxidation, and implantation.² The lessons learned, from exploring the fundamental dynamics of how an energetic particle initiates chemical change at and beyond the gas/surface interface, can impact a variety of technological applications that occur under nonthermal conditions. For example, an orbiting space vehicle is continuously exposed to a flux of energetic neutral atoms/molecules, ions, electrons, charged particle radiation, electromagnetic radiation, meteoroids, and orbital debris.³ Because silicon oxide is commonly employed as a protective transparent coating in spacecraft applications, it is critical for aerospace engineers to know how SiO_2 and other vulnerable surfaces are potentially degraded and/or eroded through prolonged exposure to 5–10-eV oxygen atoms and ions.

The oxidation of silicon has been a long-standing topic of investigation within the microelectronics industry, where it is highly desirable to grow thin gate oxides at low temperature.⁴ The thermal budget of device fabrication places a ceiling on the processing temperatures that can be employed in thin oxide-film growth before other components on the same substrate will become irreparably damaged. Plasma-assisted oxidation, plasma-enhanced chemical vapor deposition, ion-beam oxidation (IBO), and dual ion-beam deposition are attractive alternatives to thermal oxidation, because the energetic deposition of reactive oxygen species helps grow high quality oxide films without the need for high-temperature annealing.^{5–8} In the case of plasma oxidation of silicon, the application of a positive or negative 60-V potential to the substrate accelerates oxidation substantially.⁹ This demonstrates the important role of energetic ions in the oxidation process.

Low-temperature IBO exploits the energy of the incident ion to promote penetration below the surface layer and acti-

vate the transport of interstitial oxygen to the Si/SiO_x interface.¹⁰ Because silicon within the oxide layer is supplied exclusively from the substrate, an IBO film will attain a maximum thickness when the rate at which oxygen diffuses to the Si/SiO_x interface equals the rate at which the film is etched by the incident ion beam. Todorov and Fossum used a 40–120-eV ion beam (containing O^+ , O_2^+ , and Ar^+) to form 40-Å-thick oxide films on silicon at room temperature.¹¹ The electrical quality of the oxide layer was determined to be satisfactory for use as a gate dielectric in a thin-film metal-oxide-semiconductor field-effect transistor device.¹² Similarly, neutral atomic and molecular oxygen implantation at energies of 5 and 10 eV, respectively, creates a 45-Å-thick oxide layer on silicon.¹³

Quinteros *et al.* explored the intermediate stages of IBO of Si(001) by studying how 5–150-eV O^+ etches the topmost layer of the silicon oxide film, as the film is being further oxidized by the ion beam.^{14,15} The authors utilized mass-, energy-, and angular-resolved detection of the scattered product ions (O_2^- and SiO^+) along with isotopic labeling of the incident ions to characterize the competition between abstraction and sputtering mechanisms. For example, at O^+ ion energies above 16 eV, a scattering-mediated abstraction mechanism is operative. That is, the incident O^+ ion neutralizes on approach to the surface, scatters from the lattice, and picks up an oxygen atom on the outbound trajectory. At collision energies above 33 eV, a second reaction channel for O_2^- emergence appears, in which the incident projectile first creates an O-atom recoil upon impact. As the oxygen recoil leaves the surface, it abstracts a neighboring oxygen atom from the lattice to form scattered O_2^- (recoil abstraction). Studies such as this provide a detailed view of the mechanisms leading to scattered products in IBO.

In a similar vein, the present study characterizes the mechanisms for oxygen incorporation within the lattice during IBO. In a pioneering study, Kimura *et al.* employed isotopic labeling as a way to monitor the migration of interstitial oxygen within a SiO_x film, as the film grew under microwave-discharge plasma oxidation.¹⁶ We describe here an isotopic labeling approach to quantitatively measure the

rate at which oxygen is incorporated into the topmost layer of a silicon oxide film during hyperthermal O^+ and O_2^+ IBO.

II. EXPERIMENT

The experimental approach involves a monoenergetic beam of mass-selected ions directed at a well-characterized surface. The oxide films are grown and studied in an ultra-high vacuum chamber described elsewhere.¹⁵ Briefly, the apparatus consists of three differentially pumped chambers: the source and buffer chambers contain the ion transport optics, the main scattering chamber houses the surface sample and diagnostic tools, and the rotatable detector chamber contains a quadrupole mass spectrometer. The main chamber pressure rises to only 5×10^{-10} torr when the ion beam is running.

The silicon oxide thin films are grown on a Si(001) substrate. The samples are cut from *p*-doped silicon wafers (0.01- Ω cm resistivity) and prepared by wet oxidation and dipping in HF to obtain an atomically flat, H-terminated surface.¹⁷ After introducing a treated Si(001) sample into the apparatus through the load-lock chamber, the substrate is heated to 900 °C to remove the hydrogen passivation layer. X-ray photoelectron spectroscopy is used to confirm surface cleanliness (less than 1% carbon contamination), and low-energy electron diffraction verifies that the surface has undergone a (2×1) reconstruction.

IBO is conducted with an oxygen ion beam, prepared by flowing $CO(g)$ through a plasma electron impact ion source (Penning gun). Cations extracted from the Colutron plasma discharge source are accelerated to 1.5 keV, and a single-ion species is mass selected within the Wien filter. Next, the ion beam is electrostatically deflected to remove neutrals and decelerated to the final beam energy (5–100 eV). For the labeling experiments, isotopically enriched $C^{18}O_2(g)$ (spectra gases) is mixed with $Ne(g)$ to form the plasma feed gas. Mass filtration of the incident ion beam selects either $^{22}Ne^+$ or a single isotope of oxygen ($^{16}O^+$, $^{18}O^+$, $^{32}O_2^+$, or $^{36}O_2^+$) with less than 1% isotopic impurities. The $^{16}O^+$ dosing beam is spatially broadened (7-mm diameter) to oxidize a larger portion of the Si(001) substrate than is sampled by the $^{18}O^+$ or $^{36}O_2^+$ tracers (4.5-mm beam diameter). All dosing and tracer experiments are performed at $T_s = 300$ K with the ~ 10 -nA ion beam directed at 45° relative to the surface normal.

Intermittently, the isotopic composition of the topmost layer is monitored by briefly switching the incident oxygen ion beam to 60-eV $^{22}Ne^+$ (3-mm beam diameter). The sputtered $^{16}O^-$ and $^{18}O^-$ ions are collected by a quadrupole mass spectrometer, positioned at the angle of maximal signal intensity. SRIM simulations predict that the relative efficiencies, at which ^{16}O and ^{18}O are sputtered from SiO_2 by 60-eV Ne^+ projectiles, differ by only 3%.¹⁸ Hence, the fractions F of ^{16}O and ^{18}O in the topmost layer of the film can be calculated simply as

$$F_{16} = \frac{I_{16}}{I_{16} + I_{18}}, \quad F_{18} = \frac{I_{18}}{I_{16} + I_{18}}, \quad (1)$$

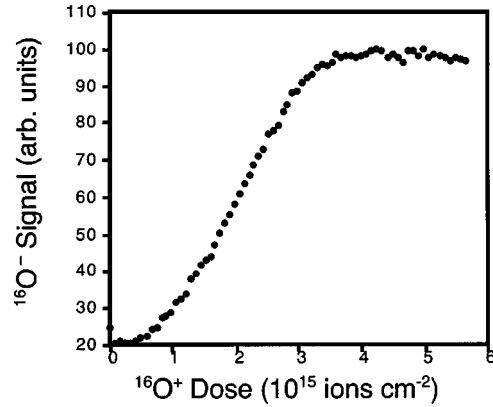


FIG. 1. The yield of scattered O^- during the initial oxidation of Si(001) with 60-eV $^{16}O^+$ at $T_s = 300$ K. After a dose of $4 \times 10^{15} O^+$ ions cm^{-2} , the chemical composition of the topmost layer of the oxide film reaches a steady state.

where I_{16} and I_{18} are the measured sputtering intensities of $^{16}O^-$ and $^{18}O^-$, respectively.

III. RESULTS

Throughout the IBO process, the growth of the oxide film on Si(001) is monitored. X-ray photoelectron spectra in the Si $2p$ region show the development of a distinct silicon dioxide Si(IV) feature and attenuation of the elemental Si(0) peak. Concurrent with the O^+ dose, scattered O^- and O_2^- products are observed in the quadrupole mass spectrometer.¹⁵ For a given incident energy, the O_2^- signal scales with the O^- signal. This indicates that the reactions leading to each product channel are equally sensitive to the nature of the oxide/vacuum interface; hence, only the scattered O^- intensity, as a function of the O^+ dose, is displayed in Fig. 1. The rapid rise in the O^- yield with the O^+ dose corresponds to the initial growth phase of the film. In the plateau region, the chemical composition of the topmost layer of the film has reached a steady state, even though the oxide layer will continue to grow as it approaches the saturation thickness (~ 40 Å). All of the data reported hereafter are collected in the steady-state regime (≥ 10 -Å thick), where the chemical nature of the oxide vacuum interface remains unchanged in time.

To measure the rate at which incident ions are incorporated into the film, an initial oxide layer is grown on Si(001) using 60-eV $^{16}O^+$, exclusively. After a steady-state oxide layer is established, a beam of 60-eV $^{18}O^+$ is targeted at the surface, and the isotopic composition of the topmost layer is monitored by periodic 60-eV Ne^+ sputtering. Figure 2 shows how the fraction [calculated from Eq. (1)] of ^{16}O and ^{18}O at the surface evolves with the $^{18}O^+$ dose. The sum of sputtered $^{16}O^-$ and $^{18}O^-$ signals remains constant throughout the experiment, confirming that the total concentration of oxygen in the topmost layer of the film is unaltered within the steady-state regime.

A simple first-order rate model is applied to the experimental data in Fig. 2. With a fixed density of oxygen sites in the topmost layer, we assume that for every ^{18}O that be-

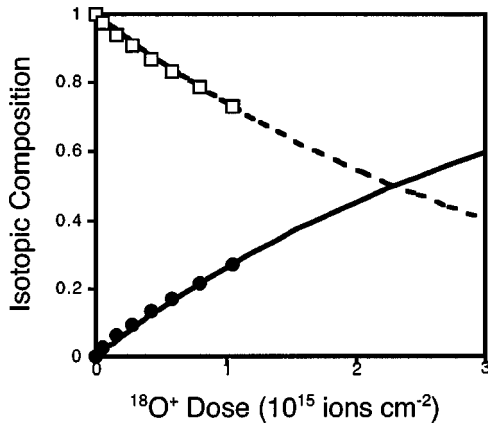


FIG. 2. The isotopic composition of the topmost layer of a Si^{16}O_x film versus the dose of 60-eV $^{18}\text{O}^+$. The fraction of ^{16}O (open squares) and ^{18}O (solid circles) in the surface layer is monitored by static secondary-ion-mass spectroscopy (SIMS) using 60-eV Ne^+ projectiles. The curves represent a fit to Eq. (3).

comes incorporated in the topmost layer, there is one less ^{16}O at the surface. The model does not differentiate whether the displaced ^{16}O goes subsurface or disappears into the vacuum. The rate at which ^{18}O is incorporated into the Si^{16}O_x lattice is proportional to the flux (J_{18}) of incident $^{18}\text{O}^+$, the instantaneous fraction (F_{16}) of surface sites occupied with ^{16}O , and a rate constant (σ):

$$\frac{dF_{18}}{dt} = J_{18}\sigma F_{16}. \quad (2)$$

Equation (2) can be easily integrated when we apply the initial condition, $F_{16}(t=0)=1$, and constrain the sum of the isotope fractions to equal unity at all times. This generates expressions for the isotopic composition,

$$F_{18} = 1 - \exp(-D_{18}\sigma), \quad F_{16} = \exp(-D_{18}\sigma), \quad (3)$$

as a function of D_{18} , the time-integrated $^{18}\text{O}^+$ flux, also known as the fluence or dose. The curves drawn through the data in Fig. 2 represent a fit to Eq. (3). The single fitting parameter σ represents the cross section for incorporation. It can be interpreted loosely as the effective area surrounding a filled oxygen site in which an incident ion must strike to replace the current oxygen atom at the site.

Experiments, such as the one shown in Fig. 2, are repeated for a range of ion kinetic energies. In each case, both the $^{16}\text{O}^+$ used to form the steady-state oxide layer and the $^{18}\text{O}^+$ employed in the incorporation step are introduced at the same kinetic energy. Figure 3 shows the cross section for $^{18}\text{O}^+$ incorporation as a function of O^+ kinetic energy. As the beam energy increases beyond 40 eV, the cross section for incorporating oxygen into the topmost layer decreases.

In a parallel set of experiments, the rate of oxygen incorporation from molecular ion projectiles is studied. Here, the steady-state Si^{16}O film is grown using $^{16}\text{O}^+$ at a selected energy. Next, the rate of ^{18}O incorporation is measured by introducing $^{36}\text{O}_2^+$ at the same kinetic energy. It was empirically verified that the steady-state regime was maintained in spite of the change in projectile. The data displayed as open

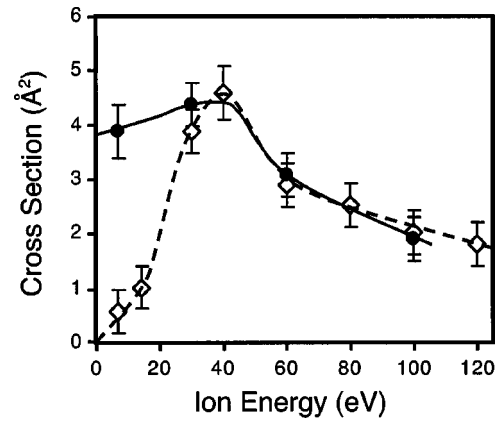


FIG. 3. The cross section for incorporation of $^{18}\text{O}^+$ (solid circles) or $^{36}\text{O}_2^+$ (open diamonds) into the topmost layer of a Si^{16}O_x film as a function of the energy of the incident ions. The cross section is scaled to the number of incident oxygen nuclei. Curves are drawn to guide the eye.

diamonds in Fig. 3 are derived from fits to Eq. (3), where the cross section σ is divided by 2 to reflect that two ^{18}O atoms are delivered by each incident $^{36}\text{O}_2^+$ projectile. The incorporation rate reaches a maximum when 40-eV $^{36}\text{O}_2^+$ impinges on the oxide layer.

The $^{36}\text{O}_2^+$ projectiles that do not trap upon impact will scatter from the Si^{16}O_x surface through one of three pathways: nonreactive scattering, dissociative scattering, or substitution. Mass-selective detection of the scattered ionic products discriminates against sputtered species ($^{16}\text{O}^-$ and $^{32}\text{O}_2^-$) in favor of those ($^{36}\text{O}_2^-$, $^{18}\text{O}^-$, and $^{34}\text{O}_2^-$) that contain nuclei originating from the incident projectile. After integrating the product ion signals over all exit velocities and scattering angles, an absolute yield is obtained. Charge-transfer dynamics strongly influence the absolute yields measured for anionic products. Thus, in an effort to extract the fundamental reaction behavior, branching ratios are calculated for the three products at each incident energy. The branching ratio for a particular anionic product is defined as the yield of the selected product divided by the sum of all three anionic product yields. Figure 4 shows the dependence of the product branching ratios on the incident $^{36}\text{O}_2^+$ energy. The threshold for dissociative scattering ($^{18}\text{O}^-$) in Fig. 4 is coincident with the onset for $^{36}\text{O}_2^+$ incorporation in Fig. 3. Moreover, the branching ratio for the substitution channel ($^{34}\text{O}_2^-$) exhibits a similar energy dependence as the cross section for $^{36}\text{O}_2^+$ incorporation.

Each data point in Fig. 3 is collected under conditions where the oxide-film growth and incorporation steps are conducted at the same ion impact energy. Consequently, it is difficult to assess whether the energy dependence to the recorded cross section is correlated primarily with the nature of the oxide (influenced by the $^{16}\text{O}^+$ growth conditions) or with the reactivity of the $^{18}\text{O}^+$ projectile. To unravel the confluence of these two effects, a series of experiments are performed where the target Si^{16}O film is grown under varied $^{16}\text{O}^+$ deposition energies; however, the incorporating $^{18}\text{O}^+$ ion is always introduced at 5-eV kinetic energy. Figure 5

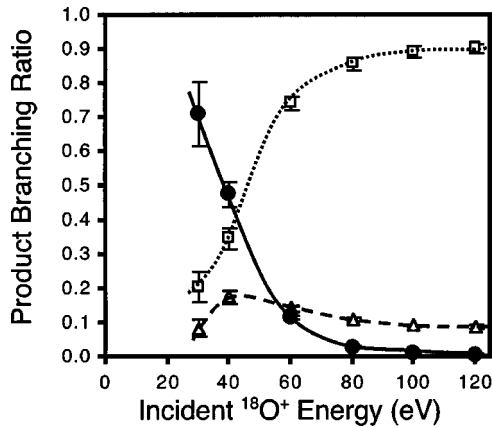


FIG. 4. Branching ratio for scattered anionic products as a function of the incident energy with which $^{36}\text{O}_2^+$ collides with Si^{16}O_x . The oxide film was prepared by dosing 60-eV $^{16}\text{O}^+$ on $\text{Si}(001)$. Nonreactive scattering ($^{36}\text{O}_2^-$), oxygen substitution ($^{34}\text{O}_2^-$), and dissociative scattering ($^{18}\text{O}^-$) are represented by solid circles, open triangles, and open squares, respectively. Curves are drawn to guide the eye.

reveals the effect that oxide growth conditions have on the rate of oxygen incorporation. The lowest cross section for $^{18}\text{O}^+$ incorporation occurs when the oxide layer is initially formed using a $^{16}\text{O}^+$ deposition energy of ~ 20 eV.

IV. DISCUSSION

The relatively large values for the incorporation cross section in Figs. 3 and 5 indicate that a facile exchange of oxygen nuclei occurs at the oxide/vacuum interface during IBO. To estimate the probability that an incident ion is incorporated into the top layer of the silicon oxide lattice, (i) the depth sensitivity of the sputtering probe and (ii) the density of the film must both be approximated.

- (i) The film's isotopic composition is probed by "gentle" secondary-ion-mass spectrometry (SIMS), i.e., the mass spectrum of sputtered O^- is recorded when 60-eV Ne^+

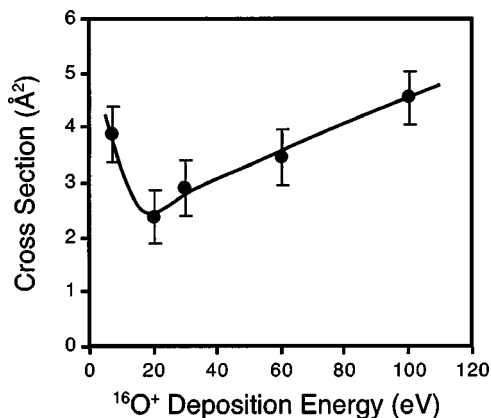


FIG. 5. The cross section for incorporation of 5-eV $^{18}\text{O}^+$ into the topmost layer of a Si^{16}O_x film versus the incident energy at which the film was originally grown by $^{16}\text{O}^+$ IBO of $\text{Si}(001)$. The curve is drawn to guide the eye.

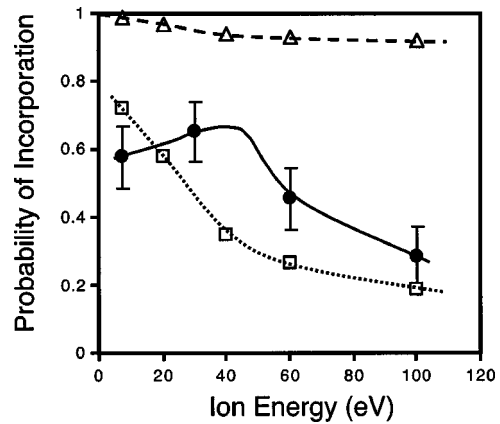


FIG. 6. The probability for incorporation of $^{18}\text{O}^+$ into Si^{16}O_x as a function of the $^{18}\text{O}^+$ kinetic energy. Experimental data (solid circles) are compared to SRIM simulations of total incorporation probability (open triangles) and predicted incorporation into the top 3.5- \AA layer (open squares) of the film. Curves are drawn to guide the eye.

projectiles bombard the surface. Smith, Harrison, Jr., and Garrison have simulated at 1–3 keV the Ar^+ sputtering $\text{Si}(110)$ and found that atoms from the first monolayer comprise 75% of the signal.^{19,20} The high displacement energy (15–25 eV) of bulk atoms precludes the contribution of second-layer atoms to the sputtered signal produced by 60-eV Ne^+ projectiles. Hence, only oxygen atoms found in the topmost layer (3.5- \AA depth) of the SiO_2 film are expected to contribute to the sputtering signal. Changes in the assumed depth of origin for sputtered oxygen will not affect the measured cross sections, because the depth of origin is always less than the oxide-film thickness (>10 \AA).¹¹

- (ii) Two approaches are adopted for estimating the density of the silicon oxide films. If we assume that the number density of oxygen in our silicon oxide film is close to that of crystalline quartz ($4.66 \times 10^{22} \text{ cm}^{-3}$), then the region of the film under study (3.5- \AA depth) contains approximately 1.62×10^{15} oxygen sites per cm^2 of surface area. Alternatively, Engstrom, Bonser, and Engel assumed that two oxygen atoms bind to each unsaturated Si atom in the early stages of oxide growth on $\text{Si}(001)$.²¹ Under this approximation, approximately 1.36×10^{15} oxygen sites exist per cm^2 of surface area. The estimations outlined above imply that the average surface area associated with each accessible oxygen site probably lies somewhere between 6.1 and 7.4 \AA^2 .

The probability that an incident $^{18}\text{O}^+$ ion is incorporated into the topmost layer of SiO_x can then be calculated from the experimentally determined incorporation cross section divided by the surface area per accessible oxygen site. This quantity is plotted versus the $^{18}\text{O}^+$ incident energy in Fig. 6 (solid circles). Approximately 30%–65% of the impinging $^{18}\text{O}^+$ projectiles come to rest in the top 3.5 \AA of the silicon oxide film. The probabilities reported in Fig. 6 are directly proportional to the choice of sensitivity depth for the Ne^+ probe; consequently, if the estimated number of O sites per

unit surface area deviates from that calculated above, the solid curve in Fig. 6 will scale proportionally.

It is difficult to accurately model this system using molecular-dynamics simulations, because the many-body potential-energy surface governing the O/SiO_x interaction is unknown. Alternatively, SRIM simulations utilize a more tractable Monte Carlo algorithm to treat sputtering, backscattering, and implantation for ions impinging on structureless solids.¹⁸ The SRIM code computes that less than 10% of the incident ¹⁸O⁺ ions are backscattered from SiO₂ (see open triangles in Fig. 6). For the fraction of oxygen projectiles that are incorporated into the lattice, SRIM predicts the distribution of implantation depths. The open squares in Fig. 6 represent the probability, as calculated from SRIM, that an incident ¹⁸O⁺ ion is incorporated into the top 3.5 Å of the lattice. The qualitative agreement between experiment (solid circles) and simulation (open squares) at ion energies above 40 eV confirm that higher-energy projectiles penetrate deeper into the lattice; those ¹⁸O projectiles that implant below 3.5 Å are not detected by the 60-eV Ne⁺ SIMS probe. For O⁺ energies less than 40 eV, it is difficult to conclude, within experimental error, whether there exists an energy dependence to the cross section for incorporation.

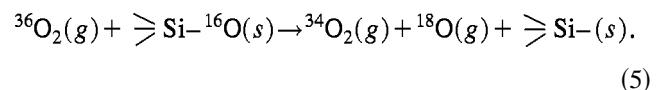
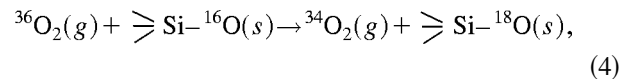
The scattered product distribution provides valuable information on the fate of the ³⁶O₂⁺ projectile. Figure 4 demonstrates that dissociative scattering (¹⁸O⁻) is unlikely at energies below 30 eV. The observed threshold for O₂ fragmentation is consistent with an impulsive dissociation mechanism, wherein the collision transfers translational energy into rovibrational energy that promptly ruptures the molecular bond.²² In contrast, dissociative neutralization can occur when electron transfer populates a repulsive potential-energy curve for the molecule. The latter process often lacks a distinct dissociation threshold because the incident energy of the projectile is only weakly coupled to the reaction coordinate. For incident ³⁶O₂⁺ energies above 40 eV, impulsive dissociation will effectively deliver pairs of atomic oxygen fragments to the surface.

Figure 3 illustrates the sensitivity of the incorporation cross section to the nature of the projectile. At incident energies below 40 eV, O⁺ is incorporated into the topmost layer of SiO_x more readily than is O₂⁺. However above 40 eV, the two projectiles exhibit similar rates of incorporation. This behavior can be explained by examining the relative reactivity and penetration depth of O⁺ versus O₂⁺. The relatively large size and lower chemical reactivity of O₂ compared to O presents a larger barrier for incorporation into the lattice. Szymanski, Stoneham, and Shluger performed *ab initio* calculations to assess the energies of various interstitial oxygen species in α-quartz.²³ They determined that a molecular oxygen interstitial is energetically more favored than two atomic oxygen interstitials, and negatively charged interstitial species are more favored than their neutral counterparts. The authors concluded that an atomic oxygen interstitial easily undergoes O-atom exchange with nondefective sites in the SiO₂ lattice; however, they predicted that interstitial O₂ is unable to dissociate or become covalently bound within the SiO₂ framework. Consequently, if an O₂ projectile

penetrates beneath the surface layer, it will adopt a negative charge but remain undissociated as it migrates to the SiO_x/Si interface, as has been shown in high-temperature dry oxidation experiments.^{16,24} In summary, the relatively low cross section for slow O₂ can be assigned to the high barrier for O₂ incorporation. This increases the probability for nonreactive scattering and extends the diffusion length of O₂ interstitials—reducing the chance of detecting ¹⁸O in the top-most layer.

In contrast, a more energetic O₂⁺ projectile will dissociate at the surface, and the nascent oxygen fragments will promptly trap and diffuse as interstitial atomic species. Atomic oxygen interstitials are likely to exchange with ¹⁶O in the lattice or, to a lesser extent, undergo geminate recombination to form a mobile O₂ interstitial.²³ At sufficiently high impact energies, O₂ will completely dissociate, and the ensuing fragments will independently incorporate into the lattice. Although the nascent fragments each possess approximately half the energy of the incident projectile, the cascade energy will scale with the incident ion energy, regardless of whether atomic or molecular projectiles are employed. Atom transport in the oxide layer is most strongly coupled to the cascade energy. Consequently, energetic O₂⁺ bombardment results in an outcome equivalent to that for two independent O⁺ projectiles. Kang, Kasi, and Rabalais observed a similar effect in the reaction of CO⁺ with Ni(111).²⁵ Whereas the reactivity of O⁺ with Ni(111) decreased monotonically with incident energy, the reaction of CO⁺ rose dramatically and peaked near 20 eV.

The appearance of scattered ³⁴O₂⁻ in Fig. 4 demonstrates that a portion of incident ³⁶O₂⁺ undergoes charge transfer and trades an ¹⁸O for ¹⁶O. Thermodynamically, a complete exchange of oxygen nuclei [Eq. (4)] is strongly favored over a partial substitution [Eq. (5)]:



Consequently, the emergence of scattered ³⁴O₂⁻ is likely to be accompanied by the incorporation of ¹⁸O into the lattice. The remarkable similarity between the branching ratio for ³⁴O₂⁻, shown in Fig. 4, and the incorporation cross section for ³⁶O₂⁺, plotted in Fig. 3, suggests that the symmetric exchange reaction [Eq. (4)] may contribute to the incorporation of molecular oxygen into SiO_x. However, the coalescence of the ³⁶O₂⁺ and ¹⁸O⁺ incorporation data at high impact energy implies that complete fragmentation of ³⁶O₂⁺ is required for both oxygen nuclei to incorporate.

Figure 5 confirms that the reactivity of 5-eV ¹⁸O⁺ with a thin Si¹⁶O_x film depends on the beam energy with which the IBO film is formed. By holding constant the energy of incorporating ¹⁸O⁺, this experiment is sensitive primarily to the

growth conditions used to initially prepare the oxide layer. The incorporation rate is lowest for films oxidized with $^{16}\text{O}^+$ at approximately 20 eV. Since oxygen incorporates most easily at defect sites, the data suggest that an oxide layer formed using 20-eV $^{16}\text{O}^+$ is created with fewer defects than a layer grown at other energies. When low deposition energies (≤ 5 eV) are employed, each incident oxygen atom sticks at the site of impact with limited mobility. This produces vacancy sites, interstitials, and other defects that are not removed by room-temperature annealing. As the ion energy is increased, the projectile's incident momentum leads to an enhanced mobility. In addition, the collision deposits a large amount of energy into a small volume of the surface, resulting in localized annealing of the nearby lattice. Together, these effects reduce the number of defect sites in the oxide layer and correspondingly diminish the cross section for incorporation. However, when the ion-deposition energy exceeds 20 eV, the projectiles can impulsively displace stable lattice atoms, thus generating new defect sites. This results in an enhanced rate of incorporation that continues to increase with additional deposition energy.

A similar phenomenon was noted by Rabalais and co-workers, who examined the homoepitaxial deposition of 8–40-eV Si^+ on $\text{Si}(001)$.^{6,26,27} They characterized the quality of their ion-deposited films by employing a battery of surface-sensitive techniques (reflection high-energy electron diffraction, Auger electron spectroscopy, high-resolution transmission-electron microscopy, Rutherford backscattering spectrometry, and atomic force microscopy). Interestingly, they found that epitaxial growth at 160 °C yielded the fewest number of defects when the film was deposited using 20-eV Si^+ . The authors argued that at lower collision energies, the impinging ion sticks to the surface without migrating to a preferred site (e.g., step edges) for layer-by-layer growth. Furthermore, ions deposited at energies above 25 eV generate stable defect sites within the film that are not annealed out under moderate surface-temperature conditions. Conse-

quently, 20 eV represents the ideal deposition energy for enhanced adatom penetration and mobility without the side effect of collision-induced damage to the film. On the basis of the experimental data and molecular-dynamics simulations, the authors concluded that the penetration and displacement thresholds for silicon deposition were 8 and 20 eV, respectively. Figure 5 reveals that it is precisely when the $^{16}\text{O}^+$ deposition energy exceeds 20 eV that the cross section for further oxygen incorporation begins to increase. The onset for generating defect sites through O^+ IBO of $\text{Si}(001)$ is consistent with the threshold for silicon atom displacement measured by Marton, Boyd, and Rabalais.²⁷

V. SUMMARY

This study presents an absolute cross section measured for incorporating hyperthermal oxygen ions into the topmost layer of a silicon oxide thin film. Experiments and simulations suggest that up to 65% of the impinging oxygen ions are incorporated within 3.5 Å of the surface. At incident energies below 40 eV, O_2^+ reacts less readily than O^+ , because without fragmentation, it is difficult for O_2 to incorporate within the SiO_x framework. As the incident energy increases, however, impulsive dissociation and/or oxygen exchange enables the O_2^+ projectile to incorporate at similar rates as O^+ . Room-temperature IBO of $\text{Si}(001)$ is ideally conducted with 20-eV O^+ , where the modest deposition energy promotes oxygen mobility without inducing significant radiation damage.

ACKNOWLEDGMENTS

This work was conducted at the University of Notre Dame through the Center for Materials Chemistry in the Space Environment, a Multidisciplinary University Research Initiative (MURI) supported by the Air Force Office of Scientific Research.

¹D. C. Jacobs, in *Chemical Dynamics in Extreme Environments*, edited by R. Dressler (World Scientific River Edge, NJ, 2001).

²D. C. Jacobs, *Annu. Rev. Phys. Chem.* **53**, 379 (2002).

³E. Murad, *Annu. Rev. Phys. Chem.* **49**, 73 (1998).

⁴D. W. Hess, *IBM J. Res. Dev.* **43**, 127 (1999).

⁵J. Stasiak, J. Batey, E. Tierney, and J. Li, *IEEE Electron Device Lett.* **10**, 245 (1989).

⁶A. H. Al-Bayati, S. S. Todorov, K. J. Boyd, D. Marton, J. W. Rabalais, and J. Kulik, *J. Vac. Sci. Technol. B* **13**, 1639 (1995).

⁷H. Shibata, S. Kimura, and H. Taktoh, *Jpn. J. Appl. Phys., Part 1* **39**, 1327 (2000).

⁸D. F. Lai, J. Robertson, and M. I. Milne, *Thin Solid Films* **383**, 220 (2001).

⁹I. Kamioka, K. G. Nakamura, T. Kawabe, and M. Kitajima, *Solid State Commun.* **97**, 531 (1996).

¹⁰J. M. E. Harper, M. Heiblum, J. L. Speidelli, and J. J. Cuomo, *J. Appl. Phys.* **52**, 4118 (1981).

¹¹S. S. Todorov and E. R. Fossum, *Appl. Phys. Lett.* **52**, 48 (1988).

¹²S. S. Todorov, S. L. Shillinger, and E. R. Fossum, *IEEE Electron Device Lett.* **8**, 468 (1986).

¹³M. Tagawa, T. Ema, H. Kinoshita, N. Ohmae, M. Umeno, and T. K. Minton, *Jpn. J. Appl. Phys., Part 2* **37**, L1455 (1998).

¹⁴C. L. Quinteros, T. Tzvetkov, and D. C. Jacobs, *J. Chem. Phys.* **113**, 5119 (2000).

¹⁵C. L. Quinteros, T. Tzvetkov, X. Qin, and D. C. Jacobs, *Nucl. Instrum. Methods Phys. Res. B* **182**, 187 (2001).

¹⁶S. Kimura, E. Murakami, T. Warabisako, E. Mitani, and H. Sunami, *J. Appl. Phys.* **63**, 4655 (1988).

¹⁷P. Dumas, Y. J. Chabal, and P. Jakob, *Surf. Sci.* **270**, 867 (1992).

¹⁸J. Ziegler, SRIM Computer code is available at no charge from <http://www.SRIM.org/>

¹⁹R. Smith, D. E. Harrison, Jr, and B. J. Garrison, *Phys. Rev. B* **40**, 93 (1989).

²⁰R. Smith, *Atomic and Ion Collisions in Solids and at Surfaces* (Cambridge University, New York, 1997).

- ²¹J. R. Engstrom, D. J. Bonser, and Thomas Engel, *Surf. Sci.* **268**, 238 (1992).
- ²²J. R. Morris, G. Kim, T. L. O. Barstis, R. Mitra, C. L. Quinteros, and D. C. Jacobs, *Nucl. Instrum. Methods Phys. Res. B* **125**, 185 (1997).
- ²³M. A. Szymanski, A. M. Stoneham, and A. Shluger, *Solid-State Electron.* **45**, 1233 (2001).
- ²⁴C. J. Han and C. R. Helms, *J. Appl. Phys.* **59**, 1767 (1986).
- ²⁵H. Kang, S. Kasi, and J. W. Rabalais, *Nucl. Instrum. Methods Phys. Res. B* **33**, 438 (1988).
- ²⁶J. W. Rabalais, A. H. Al-Bayati, K. J. Boyd, D. Marton, J. Kulik, Z. Zhang, and W. K. Chu, *Phys. Rev. B* **53**, 10 781 (1996).
- ²⁷D. Marton, K. J. Boyd, and J. W. Rabalais, *J. Vac. Sci. Technol. A* **16**, 1321 (1998).